frontiers

1

Fragmentation dynamics of fluorene explored using ultrafast XUV-Vis pump-probe spectroscopy

D. Garg [†,1,2], **J. W. L. Lee** [†,1,3], **D. S. Tikhonov** [†,1,4*], **P. Chopra** [1,4], **A. L. Steber** [1,4,5], **A. K. Lemmens** [6,7], **B. Erk** [1], **C. Passow** [1], **D. Loru** [1,4], **E. Müller** [1], **F. Allum** [3], **R. Boll** [8], **S. Düsterer** [1], **D. Heathcote** [3], **D. Ramm** [1], **D. Rompotis** [1,8], **F. Ziaee** [9], **H. Köckert** [3], **J. Lahl** [10], **J. Peschel** [10], **J. Wiese** [11,12], **L. He** [11], **M. Johny** [2,5,11], **M. M. Kazemi** [1], **P. Olshin** [13], **R. Mason** [3], **S. Gruet** [1], **S. Maclot** [10,14], **S. Trippel** [5,11], **T. Mullins** [11], **X. Cheng** [1,11], **S. Bari** [1], **M. Burt** [3], **J. Küpper** [2,5,11,12], **A. M. Rijs** [11], **D. Rolles** [9], **S. Techert** [1,15], **P. Eng-Johnsson** [10], **M. Brouard** [3], **C. Vallance** [3], **B. Manschwetus** [1], **M. Schnell** [1,4*]

[1] *Deutsches Elektronen-Synchrotron DESY, Notkestraße 85, 22607 Hamburg, Germany*
[2] *Department of Physics, Universität Hamburg, Germany*
[3] *Department of Chemistry, University of Oxford, Chemistry Research Laboratory, 12 Mansfield Rd, Oxford OX1 3TA, UK*
[4] *Institute of Physical Chemistry, Christian-Albrechts-Universität zu Kiel, Kiel, Germany*
[5] *Center for Ultrafast Imaging, Universität Hamburg, Germany*
[6] *Van't Hoff Institute for Molecular Sciences, University of Amsterdam*
[7] *Radboud University, FELIX Laboratory, The Netherlands*
[8] *European XFEL, Schenefeld, Germany*
[9] *J.R. Macdonald Laboratory, Department of Physics, Kansas State University, Manhattan, KS, USA*
[10] *Department of Physics, Lund University, Sweden*
[11] *Center for Free-Electron Laser Science, Deutsches Elektronen-Synchrotron DESY, Hamburg, Germany*
[12] *Department of Chemistry, Universität Hamburg, Germany*
[13] *Saint Petersburg State University, Saint Petersburg, Russia*
[14] *Physics Department, University of Gothenburg, Sweden*
[15] *Institute for X-Ray Physics, Georg-August-Universität, Göttingen, Germany*
† *These authors have contributed equally to this work and share first authorship.*

Correspondence*:
Melanie Schnell, Denis S. Tikhonov
melanie.schnell@desy.de, denis.tikhonov@desy.de

ABSTRACT

We report on the use of extreme ultraviolet (XUV, 30.3 nm) photons from the Free-electron LASer in Hamburg (FLASH) and visible (Vis, 405 nm) photons from an optical laser to investigate the relaxation and fragmentation dynamics of fluorene ions. The ultrashort laser pulses allow to resolve molecular processes occurring on the femtosecond timescales. Fluorene is a prototypical small polycyclic aromatic hydrocarbon (PAH). Through their infrared emission signature, PAHs have been shown to be ubiquitous in the universe and to play an important role in the chemistry of the interstellar medium. Our experiments tracked the ionization and dissociative ionization products of fluorene through time-of-flight mass spectrometry and velocity-map imaging. We disentangled multiple formation channels for each of the fragment ions and report relaxation lifetimes of the excited fluorene mono-cation and di-cation on the femtosecond timescale.

Keywords: fluorene, polycyclic aromatic hydrocarbons, mass spectrometry, velocity-map imaging, fragmentation, time-resolved spectroscopy, ultrafast dynamics, PImMS

1 INTRODUCTION

The rich molecular inventory of the interstellar medium (ISM) includes polycyclic aromatic hydrocarbons (PAHs), which are estimated to constitute more than 10% of the total galactic carbon [1, 2, 3, 4]. PAH molecules absorb far-UV photons, and they relax through IR photon emission [5]. The unidentified infrared bands (UIR), measured in the interstellar atomic hydrogen (H II) and planetary nebula regions of the ISM are attributed to the PAHs and their clusters in cationic or neutral form [6, 7, 8, 9], and are also referred to as Aromatic Infrared Bands (AIBs). With radio telescope observations, the support of laboratory experiments, and quantum chemical calculations, the first PAH (indene) and substituted PAHs (1-cyano-naphthalene and 2-cyano-naphthalene) have recently been identified in the ISM [10, 11, 12]. To understand the formation of these species, various mechanisms and hypothesis are proposed, involving small hydrocarbons or hydrogen as precursors. These small species might have became available as the fragmentation products of other PAHs under harsh radiations [12, 13, 14]. Understanding the complex pathways leading to the formation of the detected carbon-containing species extending from small-sized PAHs to large carbonaceous species (e.g. C_{60}^{+} [15]) will provide guidance towards finding more molecules and exploring the constituents of the ISM in the presence of photons, ions, and electrons. One of the ways to look into the complex chemical reactions involved in the ISM is to study the interaction of the relevant molecules with radiation at well defined wavelengths and observing the dissociation products to provide insights into the possible species present in the ISM. Knowledge of the reaction products and the average electronic relaxation lifetimes of the excited species will aid the astrochemical evolution models [11].

Despite the remarkable stability of PAHs, they can undergo ionization, isomerization, fragmentation, and dissociative ionization when exposed to high-energy radiation [16, 17, 18, 19, 20, 21]. Understanding these processes is challenging for both computational and experimental methods because a large number of nuclear and electronic degrees of freedom are strongly coupled when the system is highly excited and typically enters the non-adiabatic regime, in which the Born-Oppenheimer approximation breaks down [22, 23, 24, 25]. The excited species then relax on ultrafast timescales, which can be investigated by pump-probe spectroscopy. These ultrafast timescales are observed and reported by several previous laboratory studies [16, 18, 21, 26].

Different experimental approaches exist to investigate the fragmentation products and the fragmentation dynamics of PAHs within different energy regimes (XUV, UV, Vis, IR) [16, 17, 20, 27, 28, 29]. The general

fragmentation pattern after the interaction of these molecules with high energy photons (a few 10 eV) shows multiple hydrogen losses and a prominent carbon backbone fragmentation, which majorly involves an even number of carbon atoms. Interaction with high energy photons may lead to the double ionization of the parent molecules, and these parent di-cations dissociate into two mono-cations with the loss of zero or an even number of carbon atoms, as shown in photoelectron-photoion-photoion-coincidence (PEPIPICO) measurements [30, 31]. Other studies employing recoil-frame covariance analysis of velocity-map imaging also support this observation [16]. In the ultraviolet regime, larger PAHs (more than 32 carbon atoms) show more dehydrogenation and less carbon-carbon fragmentation [8] than the small and medium-sized PAHs, which undergo fragmentation affecting the carbon skeleton. Fragmentation of the carbon skeleton could also provide information on the origin of potential species for the hydrogen abstraction and C_2H_2 addition (HACA) model, which is widely accepted as a possible PAH growth mechanism in the photosphere of the asymptotic giant branch stars, where small hydrocarbons form large molecules and soot analogues in the ISM [8, 32].

Here, we present the results from an XUV-Vis pump-probe spectroscopy experiment on the PAH fluorene (FLU, $C_{13}H_{10}$, mass = 166 a.m.u.), which contains two aliphatic hydrogen atoms. The fluorenyl cation, which is dehydrogenated singly ionized FLU, has been reported to be formed from various other PAHs [33, 34, 35], which points towards the considerable stability of the fluorenyl cation. In a previous study, FLU molecules were irradiated with visible light (593 nm) and their charged clusters were observed to undergo photo-dehydrogenation and photo-isomerization, resulting in the formation of bowl-type structures [36]. This 'curling' mechanism was discussed as a bottom-up step to form the fullerene-type structures that are found in the interstellar medium [36]. The formation of stable large FLU clusters is also interesting in the context of the "grandPAH hypothesis", according to which only the most stable species are thought to survive in the photodissociation regions [37]. In our studies, we investigated the interaction of FLU with XUV radiation centered at 30.3 nm, which corresponds to the helium (He) II emission line. The resulting ionized system generated by the XUV radiation is then probed by 405 nm, 3.1 eV visible photons. As the dynamics occur on femtosecond (fs) timescales, we used femtosecond XUV pulses (30.3 nm, 40.9 eV) generated from FLASH [38]. The studies give insight into the relaxation, dissociation, and ionization dynamics of FLU.

2 MATERIALS AND METHODS

2.1 Experiments

The experiments were performed using the CFEL-ASG Multi Purpose (CAMP) endstation [39] at the beamline BL1 at the FLASH1 branch of the free-electron laser with a double-sided velocity-map-imaging (VMI) spectrometer installed at the CAMP endstation. We used two pulsed beams (XUV and Vis), operated at a repetition rate of 10 Hz. The XUV pulses (λ = 30.3 nm, pulse duration 80 to 90 fs (FWHM), which is estimated from the pulse length of electrons [40] using "LOLA instrument" [41]) were provided by FLASH1 with an average pulse energy of 14.5 μJ, which was then reduced to 1.4 μJ by two aluminium filters of thickness 100.9 nm (55% transmission) and 423.4 nm (28% transmission), and the five beamline mirros (resultant transmission= 0.623). The second harmonic generation output of a Ti:Sapphire optical laser, obtained using one beta-barium borate (BBO) crystal, was used as the Vis laser pulse (λ = 405 nm, pulse duration under $\sim$150 fs, which is estimated from the fundamental beam pulse duration) with a pulse energy up to $\sim$390 μJ [42].

We used the VMI setup [43, 44] to obtain the ion yields and ion momenta of the FLU parent ions (mono-, di-, and tri-cation) as well as fragment ions as a function of pump-probe delay time. FLU was purchased with 98% purity from Sigma-Aldrich and was used without any further purification. A brief description of the experimental procedure and setup (shown in figure 1) is as follows. FLU with a melting point of 116°C was heated to 200°C to produce sufficient molecules in the gas phase. The molecular beam was produced *via* supersonic expansion through a high temperature Even-Lavie pulsed valve with opening times of a few ten microseconds [45]. We used helium as a carrier gas at 1-2 bar backing pressure. After passing through a pair of skimmers, the well-collimated and internally cooled molecular beam entered the vacuum chamber and was irradiated by the two almost collinear beams (XUV and Vis pulses), which crossed each other at a small angle (∼1.5 degrees) with different delay times, Δt between them. The two pulses interact with the neutral molecules perpendicularly. The ions and electrons produced by ionization or dissociative ionization of the neutral molecules were accelerated by an electric field along two diametrically opposed flight tubes and detected at the microchannel plate (MCP) detector/phosphor detector setups in the 'top' and 'bottom' detector assemblies, respectively. In this work, only the ion data is discussed.

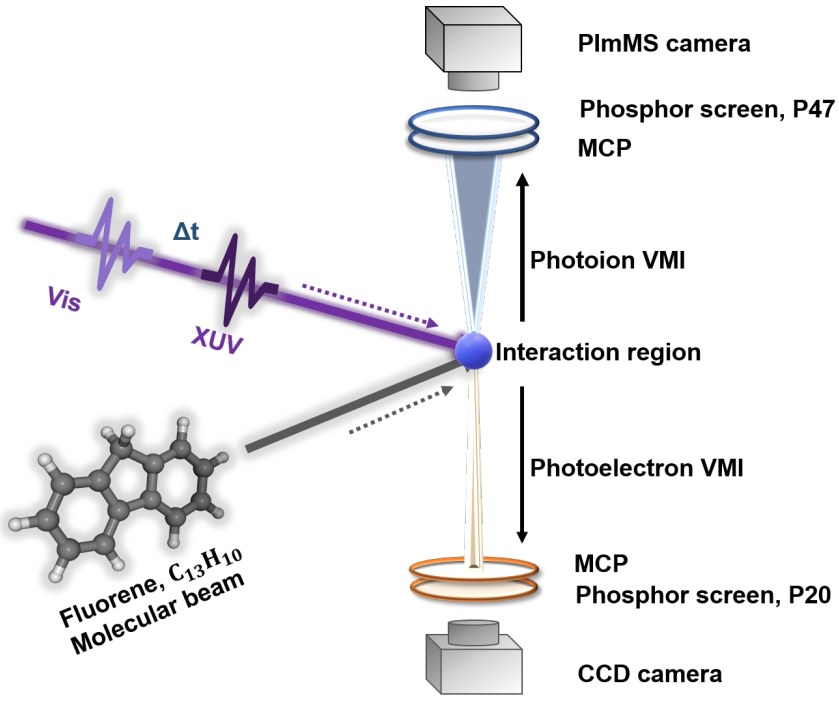

Figure 1. Schematic of the experimental arrangement at the CAMP endstation at FLASH1 (not showing the ion optics for ion and electron extraction, respectively) [39]. The supersonically expanded molecular beam interacts with the XUV and Vis pulses (arriving with a delay time, Δt between them). After interaction, ions and electrons were velocity-mapped on the ion detector assembly (at the top), and on the electron detector assembly (at the bottom). The path followed by the two beams after the interaction is not shown in the figure.

The ion detector assembly consists of a dual MCP detector coupled to a P47 phosphor screen that converts the position information of each ion hit on the detector to light. A multi-mass imaging PImMS2 sensor in a PImMS camera [46, 47] recorded the velocity-mapped 2D ion images formed by the phosphor screen for all the fragments and parent ions in each interaction event. A high-resolution TOF spectrum was obtained by recording the total signal from the MCP using a 2-GHz analog to digital converter (model: ADQ2AC-4G-MTCA, company: SP Devices). Similar to the ion detector assembly, the electrons were

simultaneously velocity-mapped onto a P20 phosphor screen and captured by a charged coupled device (CCD) camera. Each experiment involved scanning over the pump-probe delay time between the two laser pulses and recording the ion yield (intensities of the time-of-flight mass spectrum recorded) and ion momenta (extracted from the ion velocity map images) at each step. In this experiment, we scanned a range of 3 picoseconds (ps) of pump-probe delay time with 0.05 ps steps. At each delay value, 250 measurements were acquired in order to obtain sufficient statistics.

2.2 Analysis

The 2D ion velocity-map images captured from the PImMS camera were fully symmetrized (top/bottom/left/right) and then Abel-inverted to obtain the central slice of the 3D product ion velocity distributions, using the onion peeling method implemented in the PyAbel package available in Python [48, 49]. Angular integration of these Abel-inverted velocity-map ion images generated the radial distribution (in pixels), which was converted to ion momentum using a calibration factor determined through SIMION ion trajectory simulations [50]. The momentum distributions were analyzed as a function of delay time, and the resulting pump-probe delay-time dependent ion yields were fitted using in-house developed open source libraries and scripts [51, 52, 53]. The fitting procedure is explained in detail in reference [54, 55].

The temporal overlap of the two laser pulses (t_0) was extracted after simultaneously fitting eighteen different pump-probe delay time-dependent ion yield curves, recorded in an experimental event, and should have the same parameter t_0. The resulting t_0 with an accuracy of one femtosecond was then used as a constraint parameter to fit time-dependent ion yields of other fragments, which were fit with multiple transient features as discussed below for the fragment $\mathrm{C_4H_x^+}$. The pump-probe delay time values were corrected for the temporal overlap offset t_0 between the two pulses, and for jitter in the XUV pulse arrival time that was measured by the beam arrival-time monitor (BAM) [56, 57]. The ion yield intensity was also corrected for shot-to-shot FEL pulse energy fluctuations that is described briefly in the supplementary information. Covariance analysis [58] was performed on both TOF and VMI observations where TOF measurements enabled us to calculate TOF-TOF partial covariance (method is explained in detail in reference [59], and the results are shared in the supplementary information) and the two-body recoil-frame covariance could be calculated using VMI observations, which are discussed in the results section.

3 RESULTS

3.1 Time-independent results

3.1.1 Ionization and fragmentation of FLU

Mass spectra obtained after the interaction of FLU with XUV (mass spectrum in red) and Vis (mass spectrum in blue) radiation are shown in figure 2A. Subscript 'x' depicts the number of hydrogen atoms attached to the fragments (ranges from 1 to 10). In the following section, we first discuss the effect of Vis and XUV photons on FLU separately before we evaluate their combined effects.

When FLU absorbs Vis photons, mostly single ionization (ionization potential: 7.88 $\pm$ 0.05 eV [60]) with loss of up to three hydrogen atoms (hydrogen dissociation energy (approx.): $\sim$4 eV [16, 61]) and one acetylene (forming $\mathrm{C_{11}H_x^+}$) is observed. The single hydrogen atom loss from $\mathrm{FLU^+}$ is found to be the second most intense peak, $\mathrm{FLU^+}$ being the most intense one. As the energy required for ionization and dissociative ionization is more than the single Vis photon energy (3.1 eV), multi-photon processes must be involved. Consequently, several fragmentation channels are also accessible. The negligible $\mathrm{C_2H_x^+}$

peak intensity and more intense $C_{11}H_x^+$ peak in the mass spectrum indicate that the fragmentation channel producing $C_2H_x^+$ as a dissociation product from the parent mono-cation with neutral $C_{11}H_x$ is barely populated in comparison to the production of $C_{11}H_x^+$ with neutral acetylene.

The absorption of XUV photons by FLU leads to single, double, and triple ionization. The singly and doubly charged FLU ions show loss of up to three and four hydrogen atoms, respectively. In the mass spectrum, the intensity of the fluorenyl cation $C_{13}H_9^+$ is observed to be more than the intensity of $C_{13}H_{10}^+$. The major contribution of $C_{13}H_9^+$ to the mass spectrum can be attributed to the conversion of an sp^3 hybridized carbon to an sp^2 hybridized carbon after losing one hydrogen, which makes the molecule a fully conjugated system. Since XUV photons have enough energy to cause ionization and/or hydrogen dissociation, the production of the fluorenyl cation is observed to be more intense during XUV interaction than in the case of Vis pulse interaction, where the abundance of $C_{13}H_9^+$ is still less than the $C_{13}H_{10}^+$ (low abundance of the fluorenyl cation is consistent to the observation in other studies with rather low ∼4.1 eV photon energy [62] and proton impact studies [19]). Acetylene loss from the parent mono-cation forming $C_{11}H_x^+$ and from the parent di-cation forming $C_{11}H_x^{2+}$ is also observed. The abundance of $C_{11}H_x^{2+}$ is found to be higher than $C_{11}H_x^+$ that point towards a facilitated acetylene loss from the parent di-cation than from the parent mono-cation. The possible dissociation pathways leading to the formation of $C_{11}H_x^+$ and $C_{11}H_x^{2+}$ and the energies involved in dissociation of the parent mono- and di-cation are summarized in the supplementary information.

A more prominent $C_2H_x^+$ peak is observed in the XUV-only case compared to the Vis-only condition. During interaction with XUV photons, both the parent mono-cation and the di-cation can dissociate to produce $C_2H_x^+$. For the parent mono-cation, both the formation of the charged acetylene unit, $C_2H_x^+$ (together with the neutral partners, e.g. $C_{11}H_y$, where the subscript 'y' depicts the number of hydrogen atoms in the partner fragment ion), and formation of neutral C_2H_x (together with charged partners, e.g. $C_{11}H_x^+$) are feasible. The parent mono-cation dissociation will be reflected in the low momentum region, i.e., region I in figure 3, since during the dissociation of the parent mono-cation, the charged fragments are recoiling from neutral fragments. Whereas, the parent di-cation produces $C_2H_x^+$ partnered by (charged) $C_{11}H_y^+$ resulting in higher momentum and appear in region II in figure 3. The co-production of these two fragment ions is indicated by the similar momentum profiles in the region II, which is confirmed by the recoil-frame covariance (shown in figure 4). Only low amount or even no $C_2H_x^+$ is formed from FLU^+, while significant amounts are formed from the FLU^{2+}.

The differential mass spectrum is calculated by subtracting the individual ion yields observed in the XUV only and the Vis only condition from the XUV-Vis pump-probe delay-time averaged mass spectrum (shown in black in figure 2B). The positive and negative intensity show the increase and decrease in the ion yield, respectively. The decrease in the ion yield of the large fragments or the parent ion species (for example for $C_{13}H_{10}^+$, $C_{13}H_{10}^{2+}$, and $C_{11}H_8^{2+}$) together with the substantial increase in the fragment intensity allude the dissociation of the large species into the smaller fragment ions as a result of pump-probe effect.

3.1.2 Ion momenta and covariance of product fragment ions

Recoil-frame covariance analysis was performed on the multi-mass VMI data set to discern the correlated ions. The details of covariance mapping can be found in references [63, 64, 65, 66]. Briefly, recoil-frame covariance shows the velocity distribution of one ion (ion of interest) with respect to the recoil velocity vector of another ion (reference ion). Figure 4 shows the covariances between all possible mono-cation pairs resulting from dissociation of FLU^{2+}. Generally, the intense spot directing opposite to the reference ion direction indicates that the two ions (the ion of interest and the reference ion) are created from the same

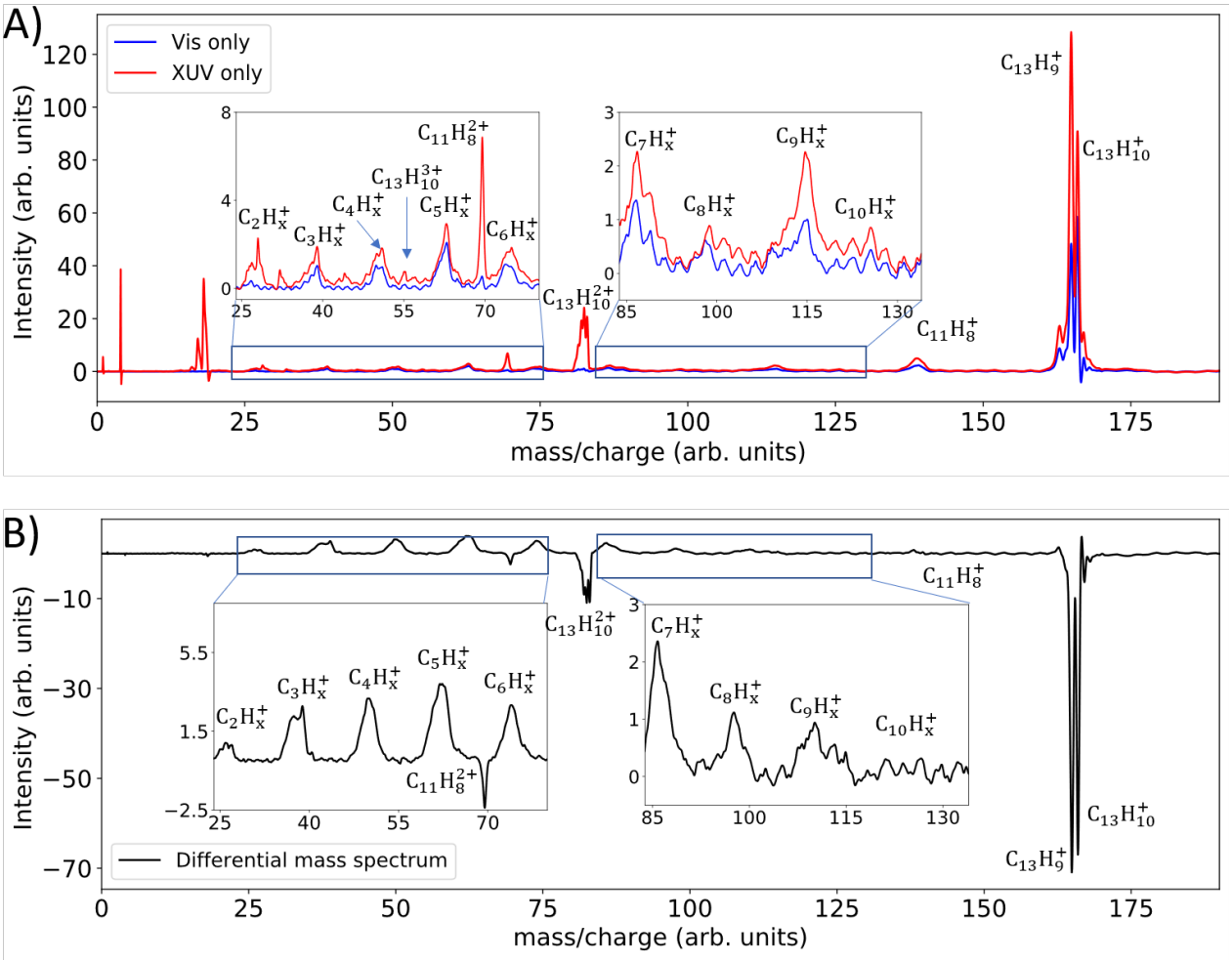

Figure 2. A) Mass spectra shown for two different conditions: XUV only (red) and Vis only (blue), which were measured using the MCP detector. The insets are the zoomed views of less intense fragments. B) Differential mass spectrum icalculated by subtracting the individual XUV only and the Vis only spectrum from the pump-probe delay-time averaged XUV-Vis mass spectrum in order to visualize the pump-probe effect.

parent molecule, in a simple two-body decay. Since recoil-frame covariance demonstrates the correlated motion of the two species, the blurred spots indicate that they are produced *via* a more complex mechanism along with other (neutral or charged) partners. It can be observed that $C_{11}H_x^+$ (green square) is only produced together with an acetylene ion, but that the acetylene ion can be produced with other mono-cations (blue rectangle). The TOF-TOF partial covariance map provides information on only three of the fragmentation channels involving dissociation of FLU^{2+} into $C_2H_x^+$ (with $C_{11}H_y^+$), $C_3H_x^+$ (with $C_{10}H_y^+$), and $C_4H_x^+$ (with $C_9H_x^+$), shown in the supplementary information. To summarize, the mass spectrum and the covariance analysis help us to identify a number of major fragmentation pathways of FLU molecules when subjected to Vis and XUV radiation. The time-dependent results are shown in the next section to understand the time evolution of the XUV-initiated dynamics in FLU molecules, probed using Vis photons.

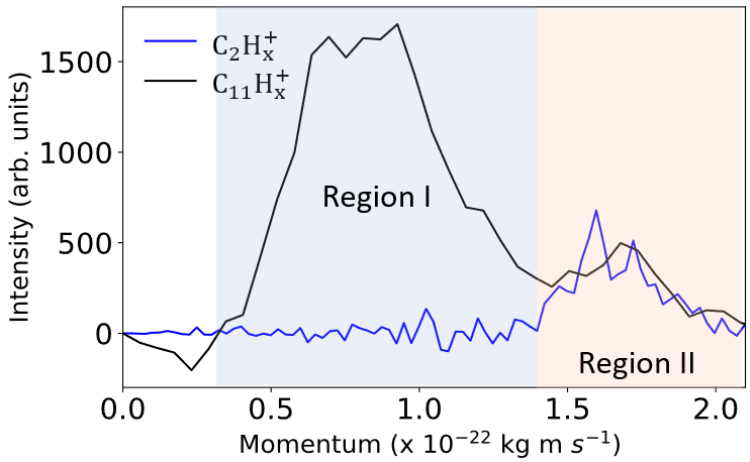

Figure 3. The momentum profiles of $C_2H_x^+$ (blue curve) and $C_{11}H_x^+$ (black curve) fragments are shown for the XUV-only condition and were acquired from the velocity-mapped ion images. Regions I and II mark ions with low and high momentum, respectively. The momentum matches for the two ions, indicating their co-production, which is confirmed by recoil-frame covariance.

3.2 Time-resolved results

3.2.1 Fragmentation channels and their relative intensities

We probed the dynamics and fragmentation pathways of fluorene initiated by the XUV photons at different delay times Δt using Vis photons. In the following, negative time delays ($\Delta t < 0$) denote Vis light irradiating the FLU molecules before the XUV pulse, and positive delays ($\Delta t > 0$) denote XUV pulses arriving earlier than Vis pulses, where the time at which the pulses are coincident corresponds to $\Delta t = 0$. In the notation (i,j), 'i' indicates the charge state of the ion of interest, and 'j' depicts the charge state of the partner produced along with the ion of interest. The (1,0) channel would thus correspond to a mono-cation (ion of interest) recoiling against a neutral partner, such products will have lower momentum than in the case of the (1,1) channel, where the mono-cation is recoiling against another mono-cation and experiences Coulomb repulsion, which is absent when recoiling against a neutral partner. We specify $C_2H_x^+$, $C_3H_x^+$, $C_4H_x^+$ as small fragments, $C_{10}H_x^+$ and $C_{11}H_x^+$ as large fragments, and the others are considered as medium fragments.

Figure 5A shows the delay-time averaged velocity-map ion images for two fragments $C_4H_x^+$ and $C_9H_y^+$. These images were processed to obtain the momentum distribution as a function of delay time shown in figure 5B, which can be divided into three channels: (1,0), (1,1), and (1,2) to depict low, medium, and high momentum regions, respectively. The signal intensity is then integrated over the momentum coordinate to generate pump-probe delay time-dependent ion yields in these distinct channels (green points in figure 6C and 6D).

FLU undergoes single and double ionization upon interaction with XUV photons, the resulting parent mono-cation and the di-cation interact with the Vis probe pulse and dissociate into the (1,0) and (1,1) channels of the fragment ions, respectively. This dissociation is evident by a sudden decrease in signal for the parent ions accompanied by an increase in the intensity of fragment ions after $\Delta t = 0$. For small fragments, the (1,1) channel is observed to be the most dominant amongst the (1,0), (1,1) and (1,2) channels as shown in figure 5B for $C_4H_x^+$. On the contrary, the medium-sized fragments are observed to be mostly produced through the (1,0) channel, shown in figure 5B for $C_9H_y^+$. The preference of the (1,0) channel and

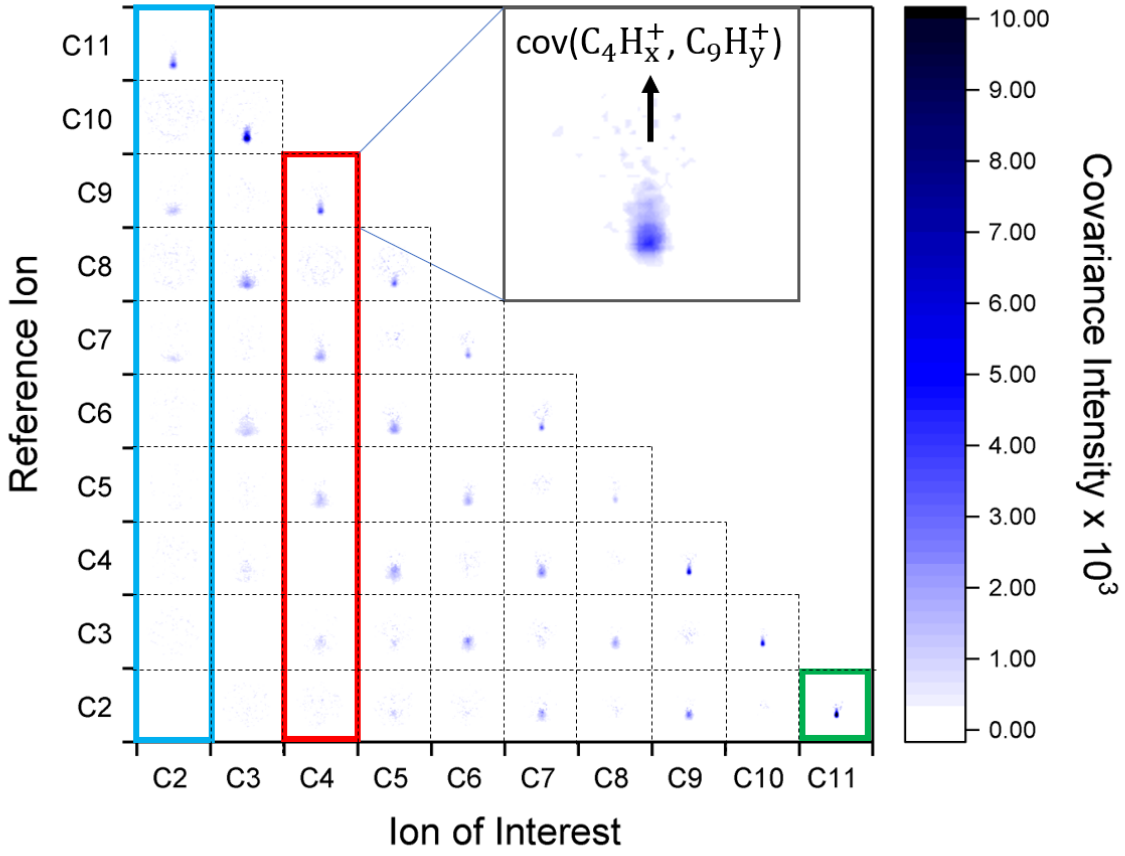

Figure 4. Each square in the dotted grid represents two-body recoil frame covariance map of the ion of interest with respect to the reference ion, for all the fragment ions, where the direction of the reference ion is vertically upward as also shown in the inset by the black arrow. Self-covariance of an ion with itself is omitted for clarity. Since FLU has thirteen carbon atoms, the sum of carbon atoms of the dissociation products can not exceed thirteen, and therefore no covariance is expected in the upper half triangle. As an example, the zoomed covariance signal of $C_4H_x^+$ with the reference ion $C_9H_y^+$ is displayed in the inset. The additional subscript 'y' depicts the number of hydrogen atoms attached to the fragment, which is the momentum partner of another fragment with number of hydrogen atoms depicted with subscript 'x'. The blue rectangle depicts multiple possible ions with which $C_2H_x^+$ could be produced, similarly the red rectangle and green square highlight the possible partners of $C_4H_x^+$ and $C_{11}H_x^+$, respectively.

(1,1) channel by medium and small-sized ions, respectively, is explained as follows. During the dissociation of the parent mono-cation, the charge is mostly carried by the larger fragment than the smaller fragment due to higher ionization potential energy of the smaller fragment. As a result, the medium-sized fragments carry away the charges, and are produced with neutrals in the (1,0) channel. The dissociation of the parent di-cation into the (1,1) channel is energetically favorable, which results in the production of small fragment ions in the (1,1) channel. Therefore, small charged ions are preferably produced with other medium-sized ions in the (1,1) channel than being produced in the (1,0) channel. Although the medium-sized ions are being produced through both channels (1,0) and (1,1), the (1,0) channel is observed to be more pronounced because of the larger production of the parent mono-cations as shown in figure 5B. A similar trend in the

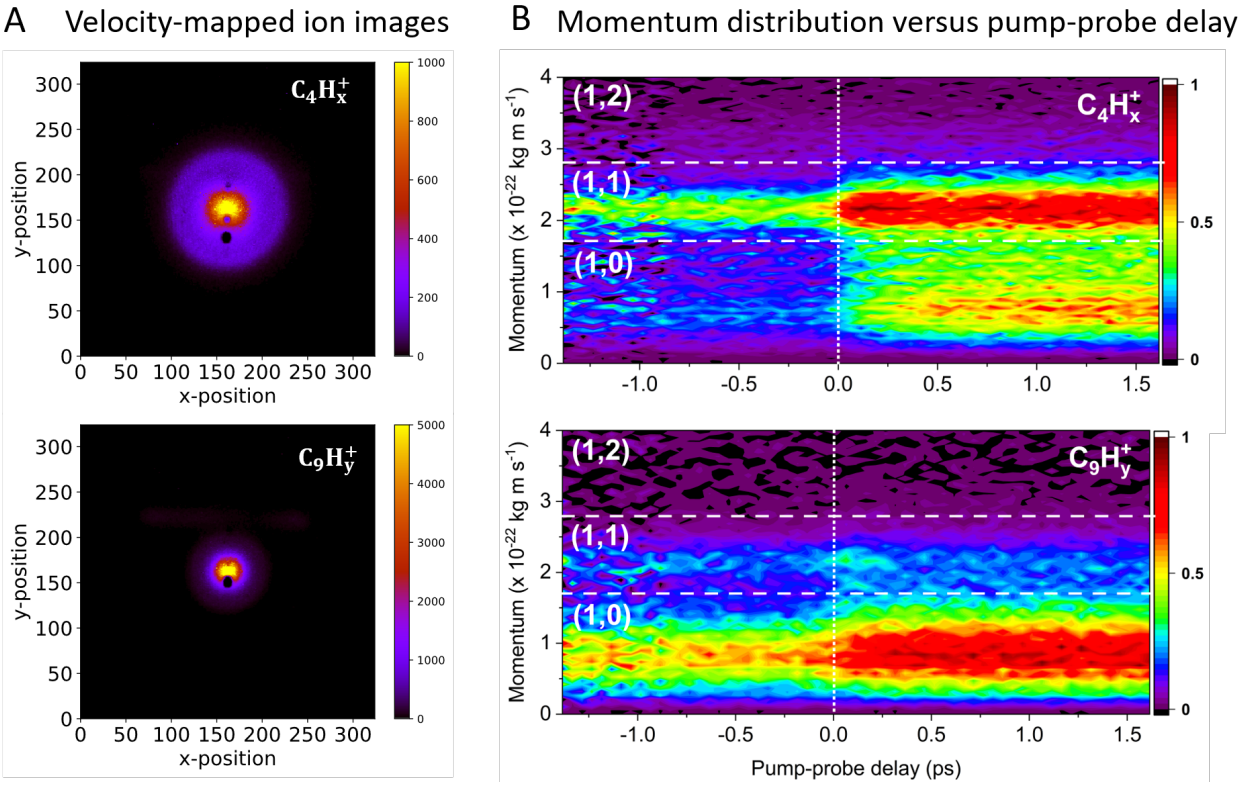

Figure 5. Results for two of the fragments, $C_4H_x^+$ and $C_9H_y^+$: A) 2D raw velocity-mapped ion images for the two fragments. The x and y axes denote the pixels of the PImMS camera (324 × 324). The visible black spots in the ion images are due to an artifact in the MCP detector. These images are later fully symmetrized and then Abel-inverted to obtain the central slice of the 3D velocity distribution. This central slice is angularly integrated, and the resultant momentum distribution is plotted as a function of delay-time shown in (B). B) Momentum distribution as a function of pump-probe delay for two fragment ions showing momentum matching in the (1,1) channel, indicating their co-production in the same fragmentation reaction, which is verified by the two-body recoil frame covariance. The white vertical dotted line indicates the overlap of the two pulses at t_0.

preference of the channels is shown in the supplementary information for other small and medium-sized fragments.

3.2.2 Internal relaxation lifetimes

The experimental delay-time dependent ion yields are shown with green points in figure 6C and 6D. The black curve shows the final fitted result, which has two major components, namely the step function (magenta curve) and transient peaks (blue, orange, and brown curves). The step function corresponds to the transition from the Vis-pump/XUV-probe (negative Δt) regime to the XUV-pump/Vis-probe (positive Δt) regime. The pronounced increase/decrease in the ion yields are depicted by transient peaks, which are observed in the positive Δt regions, i.e., we observed transient features when the FLU molecules are first pumped by the XUV photons to the singly and doubly ionized states, and the resulting parent mono-cations and di-cations dissociate through a number of fragmentation pathways after interaction with Vis pulses. The various fragmentation channels arise from different ensembles of electronic states, giving rise to different relaxation lifetimes for each channel. In the following, we address the average electronic relaxation lifetimes of FLU mono-cation and di-cation obtained from the data on dissociation into $C_4H_x^+$

through the (1,0) and (1,1) channel. The $C_4H_x^+$ ion is highlighted as an example, which shows all the features observed across the other fragment ions.

FLU^{+*}: After absorbing an XUV photon, the FLU mono-cation may be formed in electronically excited states (FLU^{+*}), which relaxes over time to low-lying electronic states depicted as FLU^+. The relaxation process is probed using Vis pulses, as shown schematically in figure 6A. Near t_0, FLU^{+*} may undergo two processes, denoted by pathways (1) and (2). The Vis pulse may induce dissociative ionization, promoting FLU^{+*} to FLU^{2+*} that dissociates into $C_4H_x^+$ and $C_9H_y^+$ (the (1,1) channel of $C_4H_x^+$), demonstrated by pathway (1) following the blue arrows. As a side note, $C_4H_x^+$ could also be produced with other mono-cations in a (1,1,0) channel with neutral co-fragments. Another possibility is that FLU^{+*} can spontaneously dissociate through the (1,0) channel of $C_4H_x^+$ before the arrival of the probe pulse. The Vis pulse can ionize the neutral fragments produced in the (1,0) channel of $C_4H_x^+$, and convert the (1,0) channel to a (1,1) channel as indicated by pathway (2) following the green arrows. During this conversion, the two charged fragments in the resulting (1,1) channel are still close enough to face a strong Coulombic repulsion, and must appear in the (1,1) channel region of the momentum distribution. Upon arrival of the Vis pulse during the evolution of the system along pathway (2), the (1,0) channel can in principle also lead to a (2,0) channel, if the Vis pulse ionizes the charged fragment ($C_4H_x^+$) rather than the neutral C_9H_y, thus there may also be a conversion from the (1,0) to the (2,0) channel. Since double ionization of the small fragment is relatively less probable and we do not observe this conversion, this process is not discussed here and is not included in the schematic. At longer delay, the FLU^{+*} electronically relaxes (orange arrow in figure 6A), and the Vis pulses can only lead to dissociation of relaxed FLU^+ through the (1,0) channel (pathway (3)).

Overall, these three pathways contribute to the transient increase in the (1,1) channel of $C_4H_x^+$ (blue peak 2 in figure 6D), which is accompanied with the transient decrease in the (1,0) channel of the $C_4H_x^+$ yield (blue peak 1 in figure 6C) near time $\Delta t = 0$. The timescales of the transient peaks correspond to the relaxation lifetime of the FLU^{+*} electronic states which lead to the formation of $C_4H_x^+$ in the channels described above. These lifetimes are found to be 249 ± 10 fs and 339 ± 77 fs, for the depletion of the (1,0) (pathway (3)) and increase in the (1,1) channel (pathway (1) and (2)) in figure 6A, respectively. In addition to relaxation *via* carbon loss fragmentation channels, the H-loss channel also shows a transient increase, with a relaxation lifetime of 136 ± 7 fs. All other fragments have similar transient increase and decrease features in their (1,1) and (1,0) channels, respectively, except $C_2H_x^+$, where the data had a significant N_2^+ contamination. These are shown in the supplementary information.

FLU^{2+*}: XUV photon absorption also forms FLU in an electronically excited di-cation state, FLU^{2+*}. Similar to the processes described above, near t_0 we probe a number of dissociative pathways. Pathway (4) demonstrates dissociative ionization of FLU^{2+*} after interaction with Vis photons forming FLU^{3+*}, which dissociates through either (1,2) or (1,1,1) channels (mono-cation recoiling against two other mono-cations), shown in figure 6B following the blue arrows. The other pathway (5) depicts spontaneous dissociation of the FLU^{2+*} ions into the (1,1) channel, before the arrival of the Vis pulse. The Vis pulse may lead to the formation of the (1,2) or (1,1,1) channel of $C_4H_x^+$. If alternatively there is a sufficiently long delay time, the FLU^{2+*} molecules relax to FLU^{2+}, and promotion to the next ionization state by the Vis pulse is less favoured. The relaxed FLU^{2+} can then dissociate through the (1,1) channel upon arrival of the Vis pulse.

We observed two peaks depicting transient depletion in the ion yields in the (1,1) channel of $C_4H_x^+$, indicated as peak 1 (brown) and peak 3 (orange) in figure 6D. The less intense peak 1 corresponds to a short lifetime of 30 ± 14 fs showing the depletion in the ion yield near t_0. This depletion is attributed to the corresponding transient increase in the (1,2) channel of $C_4H_x^+$. In our experiments, the signal for the (1,2) channel is very low, and the corresponding increase in the (1,2) channel is not observed clearly. But, the

presence of (1,2) channel for another fragment ion $C_3H_x^+$ was visible in a previous study with a different probe, and a similar short lifetime of 17 $\pm$ 5 fs was reported [16].

Peak 3 with a long lifetime of 1,001 $\pm$ 204 fs can be attributed to the formation of (1,1,1) channel. Vis pulse initiated formation of the (1,1,1) channel involves production of three fragment ions, which can be produced at any time after the Vis pulse interaction. This leads to their production in a longer time span resulting in longer lifetime. The corresponding increase in the (1,1,1) channel can not be shown since this channel will have a large momentum distribution that could not be disentangled through the momentum maps. To summarize, the relaxation lifetime of FLU^{2+*} is determined *via* three pathways (4), (5), and (6), which result in transient depletion in the (1,1) channel resolvable for conversion into two dissociation channels namely: (1,2) channel with a lifetime of 30 $\pm$ 14 fs and (1,1,1) channel with a lifetime of 1,001 $\pm$ 204 fs.

In addition to the FLU^{2+*} lifetimes obtained through the carbon skeleton fragmentation channels, we also obtained the relaxation lifetime of the FLU di-cation dissociating through the H-loss channel, which was found to be 117 $\pm$ 6 fs. The H-loss relaxation lifetimes of FLU^{2+*} and FLU^{+*} are similar and indicate that hydrogen loss from the parent ion, which involves σ-bond fission is unaffected by the difference in the charge states that are mostly localized in the conjugated-π system. The lifetimes extracted from other fragments are tabulated in the supplementary information.

The fragment ions with higher masses than $C_6H_x^+$ were fitted with only one transient increase peak. The absence of multiple peaks in the (1,1) channels for these heavier mass fragments is attributed to the following two reasons. Firstly, the conversion from the (1,1) channel to the (1,2) channel for the higher masses might be inaccessible since the small partner ions of these large fragments are difficult to doubly ionize by the Vis pulse, due to the higher ionization potential compared to the larger fragments and even higher double ionization potential. Secondly, the (1,1,1) channel is formed by the dissociation of the FLU tri-cation into smaller fragments, and hence this channel is likely to have a significantly smaller branching ratio due to the fact that one of the fragments is already large.

Relaxation lifetimes for near-ionization-threshold electronic states of FLU^{2+*} could also be extracted from the transient increase in the FLU tri-cation signal. As depicted in process (4) in the schematic of figure 6B, the Vis pulse absorption by FLU^{2+*} results in the formation of FLU tri-cation, observed as a transient increase in the FLU^{3+} ion yield. This transient peak corresponds to a relaxation lifetime of 184 $\pm$ 44 fs, which was measured using 405 nm Vis photons as the probe pulse (390 μJ pulse energy). The relaxation lifetime was also determined before using XUV-IR (30.3 nm and 810 nm) [16] pump-probe studies to be 126 $\pm$ 16 fs, which is somewhat lower compared to the XUV-Vis studies reported here.

4 DISCUSSION

Effect of fragment size on the observed relaxation lifetimes: The relaxation of the electronically excited FLU mono-cation and di-cation is probed *via* Vis pulses by inducing dissociation and/or dissociative ionization. Various fragment ions thus produced would show different relaxation lifetimes (τ_r) of FLU^+ and FLU^{2+}. The effect of the fragment ion's size on the τ_r can be observed in figure 7A and 7B, where we plot the identified relaxation lifetimes as a function of the number of carbon atoms in the fragment ion. The respective τ_r of FLU^{+*} determined through the (1,0) channel and the (1,1) channel are depicted by the blue curves in figure 7A and 7B. The small fragments with number of carbons atoms from two to eight indicate similar lifetimes (τ_r) whereas the large fragments $C_9H_x^+$ and $C_{10}H_x^+$ except $C_{11}H_x^+$ show longer τ_r.

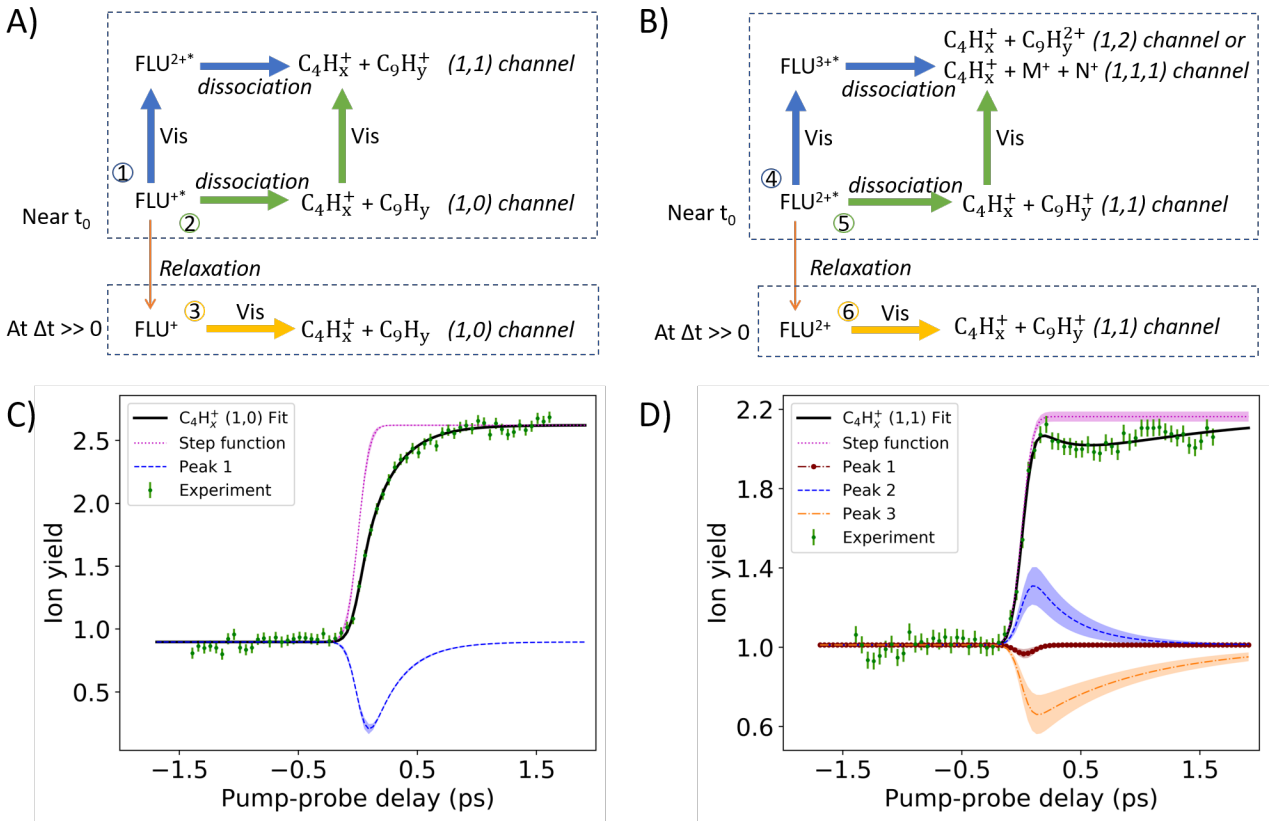

Figure 6. Schematics of the XUV-pump, Vis-probe regime for the mono-cation and di-cation, (A) and (B), respectively. The orange arrow depicts the relaxation of electronically excited ions over time. The letters M and N depict other possible fragments, which may be produced with the fragment $C_4H_x^+$. Ion yield dependence on the pump-probe delay time for the fragment ion $C_4H_x^+$ is shown for both (1,0) (C) and (1,1) channel (D). The black curve is the final fitted curve, which is the resultant of transient peaks (blue, brown, and orange) and the step function (magenta curve). In all the curves the shaded area depicts the error. C) The downward transient peak in the (1,0) channel depicts the transient depletion in the ion yield. D) The (1,1) channel is fitted with three transient features, which comprises of two peaks showing transient decrease in the ion yields (peak 1 and peak 3) and one peak indicating transient increase (peak 2).

The longer and shorter relaxation lifetimes for the small and large fragments, respectively, can be explained as follows: as can be inferred from the covariance maps (figure 4), the smaller fragments have more possible dissociation partners, and hence more fragmentation pathways are associated with them. The relaxation of FLU^{+*} into these multiple pathways, involving the formation of a small fragment with various other partners is not completely resolvable. The resultant transient peaks thus have contributions from all the possible formation pathways, and hence longer lifetimes are observed compared to the large fragments having relatively less number of formation pathways resulting in shorter lifetimes.

The exceptional longer lifetime of the $C_{11}H_x^+$ fragment ion is attributed to the fact that the formation pathway involves acetylene loss from the parent species. This pathway is thought to progress *via* a mechanism involving rearrangement of the rings to allow easy C_2H_2 loss [67], which is not the case for the C_3H_x loss or C_4H_x loss. This low-energy dissociative pathway forming $C_{11}H_x^+$ is likely to be initiated by the Vis pulse from a wide range of electronic states of FLU^+, which results in longer relaxation lifetimes. The relaxation lifetimes of the FLU^{2+*} was obtained from the shift of population from the (1,1) channel to (1,2) and (1,1,1) channel of small fragment ions. The absence of these features in the large fragments was

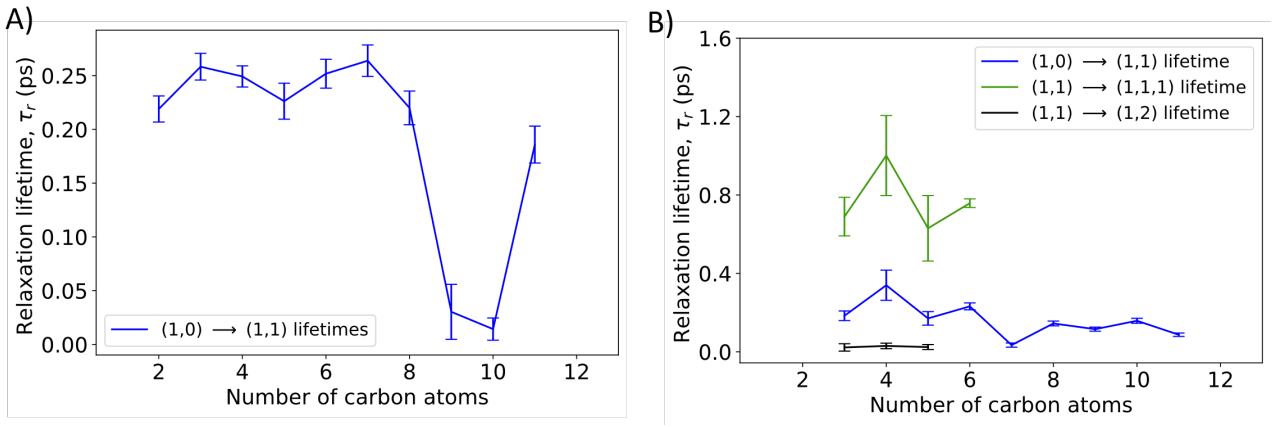

Figure 7. Observed trends as a function of fragment size. A) Relaxation lifetime of FLU^{+*} plotted as a function of the number of carbon atoms of the fragment, with which the relaxation lifetime is associated. This demonstrates the depletion of the (1,0) channel and the formation of the (1,1) channel. B) Relaxation lifetime of FLU mono-cation and di-cation plotted as a function of the number of carbon atoms of the fragment obtained from the (1,1) channel, depicting three processes. First, conversion of (1,0) channel to (1,1) channel, which correspond to the electronic relaxation lifetimes of the FLU mono-cation (blue curve). Second, conversion of (1,1) channel to (1,2) channel, which correspond to the electronic relaxation lifetimes of the FLU di-cation (black curve). Third, conversion of (1,1) channel to (1,1,1) channel, which also correspond to the electronic relaxation lifetimes of the FLU di-cation (green curve). The fragment ion $C_2H_x^+$ with a lifetime of 2.987 $\pm$ 0.006 ps, which would be on the blue curve, has been omitted for better visibility of other fragments with much shorter lifetimes.

explained in the previous section. The observation of similar lifetimes for small fragments is consistent here as depicted by the green and black curve in the figure 7B.

Effect of probe pulse on the observed relaxation lifetimes: As reported in the results section, the relaxation lifetimes of FLU^{2+*} is found to be different when probed with IR and Vis pulses. This difference in the recorded lifetime with the Vis pulse is attributed to its higher probe energy, which is able to excite lower-lying states of FLU^{2+*} to FLU^{3+*}, resulting in an increase in the observed relaxation lifetimes.

5 SUMMARY AND CONCLUSION

We studied the interaction of FLU molecules with the XUV radiation, which is present in the interstellar medium as He II emission line. FLU is observed to undergo numerous processes, involving single and double ionization, dominant single dehydrogenation post single ionization, and fragmentation into various carbon loss channels with acetylene loss being a major process. The fragments observed in the mass spectrum can be thought of as potential ions that would be present in the ISM.

Interaction with high energy photons opens the possibility for parent ion dissociation through a large number of fragmentation pathways. The momentum resolution provided by the velocity map imaging made it possible to distinguish between several channels for all the fragments, which we label as (1,0), (1,1) and (1,2) channels. A detailed analysis on the fragments showed the transient depletion and enhancement of the ion yields, as a result of FLU^{+*} and FLU^{2+*} ions' temporal relaxation into different energy levels. It is interesting to observe the time-resolved shift of the population from one channel to another one of the observed fragments, revealing the lifetimes of the species they are formed from. The results enabled us to determine the dependence of the relaxation lifetimes on the fragment size. These relaxation lifetimes are

found to be in the range of 10 fs to a few ps. The range is similar to the lifetimes that were reported in the range of 10 to 100 fs using XUV-IR pump-probe spectroscopy [16, 18, 26].

Overall, this work used an experimental and analytical tool for gaining a better understanding of the complex molecular fragmentation and dynamics in the beyond Born-Oppenheimer approximation for large systems that are astrochemically relevant and difficult to approach theoretically.

ACKNOWLEDGMENTS

This work was supported by the ERC Starting Grant ASTROROT, grant number 638027, and the project CALIPSOplus under the grant agreement 730872 from the EU Framework Programme for Research and Innovation HORIZON 2020. The experimental parts of this research were carried out at beamline BL1 FLASH at DESY, a member of the Helmholtz Association (HGF). Beamtime was allocated for proposal F-20170540. We acknowledge the Max Planck Society for funding the development and the initial operation of the CAMP end-station within the Max Planck Advanced Study Group at CFEL and for providing this equipment for CAMP@FLASH. The installation of CAMP@FLASH was partially funded by the BMBF grants 05K10KT2, 05K13KT2, 05K16KT3 and 05K10KTB from FSP-302. We acknowledge financial support by the European Union's Horizon 2020 research and innovation program under the Marie Skłodowska-Curie Grant Agreement 641789 "Molecular Electron Dynamics investigated by Intense Fields and Attosecond Pulses" (MEDEA), the Clusters of Excellence "Center for Ultrafast Imaging" (CUI, EXC 1074, ID 194651731), the "Advanced Imaging of Matter" (AIM, EXC 2056, ID 390715994) of the Deutsche Forschungsgemeinschaft (DFG), the European Research Council under the European Union's Seventh Framework Programme (FP7/2007-2013) through the Consolidator Grant COMOTION (614507), and the Helmholtz Gemeinschaft through the "Impuls-und Vernetzungsfonds". In addition, the project was supported by The Netherlands Organization for Scientific Research (NWO) and is part of the Dutch Astrochemistry Network (DAN) II (Project No. 648.000.029). P. E.-J., S. M. and J. P. acknowledge support from the Swedish Research Council and the Swedish Foundation for Strategic Research. **J. L. was supported by the European Union's Horizon 2020 research and innovation program under the Marie Sklodowska-Curie Grant Agreement No. 641789 MEDEA.** The authors are additionally thankful for support from the following funding bodies: the UK EPSRC (M. Brouard and C.V. - EP/L005913/1 and EP/V026690/1; M. Burt - EP/S028617/1), STFC (PNPAS award and mini-IPS Grant No. ST/J002895/1), the Chemical Sciences, Geosciences, and Biosciences Division, Office of Basic Energy Sciences, Office of Science, US Department of Energy (F.Z. - DE-FG02-86ER13491); the National Science Foundation (D. Rolles - PHYS-1753324); and the Helmholtz Initiative and Networking Fund through the Young Investigators Group Program (S.B.). We acknowledge the use of the Maxwell computational resources operated at Deutsches Elektronen-Synchrotron DESY, Hamburg, Germany.

AUTHOR CONTRIBUTIONS

BM and MS conceived and designed the experiments. JWLL, PC, SM, AS, SG, FA, RB, XC, SD, BE, LH, DH, MJ, MK, HK, JL, AL, DL, RM, EM, TM, PO, CP, JP, DRa, DRom, STr, JW, FZ, SB, MBu, DRol, STe, PJ, BM and MS performed the experiments. DG, JWLL, DT, PC, SM, AS, SG, and EM analyzed the data. DG, JWLL, DT, PC, AS, FA, MBu, JK, AR, DRol, PJ, MBr, CV, BM and MS performed detailed discussions of the results. DG, JWLL, DT, MS wrote the manuscript.

REFERENCES

[1] Ehrenfreund P, Sephton MA. Carbon molecules in space: from astrochemistry to astrobiology. *Faraday Discussions* **133** (2006) 277. doi:10.1039/b517676j.

[2] Herbst E, van Dishoeck EF. Complex organic interstellar molecules. *Annual Review of Astronomy and Astrophysics* **47** (2009) 427–480. doi:10.1146/annurev-astro-082708-101654.

[3] Tielens A. Interstellar polycyclic aromatic hydrocarbon molecules. *Annual Review of Astronomy and Astrophysics* **46** (2008) 289–337. doi:10.1146/annurev.astro.46.060407.145211.

[4] Ziurys LM. The chemistry in circumstellar envelopes of evolved stars: Following the origin of the elements to the origin of life. *Proceedings of the National Academy of Sciences* **103** (2006) 12274–12279. doi:10.1073/pnas.0602277103.

[5] Allamandola LJ, Tielens GGM, Barker JR. Interstellar polycyclic aromatic hydrocarbons - the infrared emission bands, the excitation/emission mechanism, and the astrophysical implications. *The Astrophysical Journal Supplement Series* **71** (1989) 733. doi:10.1086/191396.

[6] Berné O, Joblin C, Rapacioli M, Thomas J, Cuillandre JC, Deville Y. Extended red emission and the evolution of carbonaceous nanograins in NGC 7023. *Astronomy & Astrophysics* **479** (2008) L41–L44. doi:10.1051/0004-6361:20079158.

[7] Rapacioli M, Joblin C, Boissel P. Spectroscopy of polycyclic aromatic hydrocarbons and very small grains in photodissociation regions. *Astronomy & Astrophysics* **429** (2004) 193–204. doi:10.1051/0004-6361:20041247.

[8] Tielens AGGM. The aromatic universe. *Molecular Astrophysics* (Cambridge University Press) (2021), 567–628. doi:10.1017/9781316718490.013.

[9] Peeters, E, Hony, S, Van Kerckhoven, C, Tielens, A G G M, Allamandola, L J, Hudgins, D M, et al. The rich 6 to 9 μm spectrum of interstellar PAHs. *A&A* **390** (2002) 1089–1113. doi:10.1051/0004-6361:20020773.

[10] Cernicharo J, Agúndez M, Cabezas C, Tercero B, Marcelino N, Pardo JR, et al. Pure hydrocarbon cycles in TMC-1: Discovery of ethynyl cyclopropenylidene, cyclopentadiene, and indene. *Astronomy & Astrophysics* **649** (2021) L15. doi:10.1051/0004-6361/202141156.

[11] Burkhardt AM, Lee KLK, Changala PB, Shingledecker CN, Cooke IR, Loomis RA, et al. Discovery of the pure polycyclic aromatic hydrocarbon indene (c-C9H8) with GOTHAM observations of TMC-1. *The Astrophysical Journal Letters* **913** (2021) L18. doi:10.3847/2041-8213/abfd3a.

[12] McGuire BA, Loomis RA, Burkhardt AM, Lee KLK, Shingledecker CN, Charnley SB, et al. Detection of two interstellar polycyclic aromatic hydrocarbons via spectral matched filtering. *Science* **371** (2021) 1265–1269. doi:10.1126/science.abb7535.

[13] Doddipatla S, Galimova GR, Wei H, Thomas AM, He C, Yang Z, et al. Low-temperature gas-phase formation of indene in the interstellar medium. *Science Advances* **7** (2021). doi:10.1126/sciadv.abd4044.

[14] Kaiser RI, Parker DS, Mebel AM. Reaction dynamics in astrochemistry: Low-temperature pathways to polycyclic aromatic hydrocarbons in the interstellar medium. *Annual Review of Physical Chemistry* **66** (2015) 43–67. doi:10.1146/annurev-physchem-040214-121502.

[15] Campbell EK, Holz M, Gerlich D, Maier JP. Laboratory confirmation of c_{60}^+ as the carrier of two diffuse interstellar bands. *Nature* **523** (2015) 322–323. doi:10.1038/nature14566.

[16] Lee JWL, Tikhonov DS, Chopra P, Maclot S, Steber AL, Gruet S, et al. Time-resolved relaxation and fragmentation of polycyclic aromatic hydrocarbons investigated in the ultrafast XUV-IR regime. *Nature Communications* **12** (2021). doi:10.1038/s41467-021-26193-z.

[17] Robson L, Tasker A, Ledingham K, McKenna P, McCanny T, Kosmidis C, et al. Ionisation and fragmentation dynamics of laser desorbed polycyclic aromatic hydrocarbons using femtosecond and nanosecond post-ionisation. *International Journal of Mass Spectrometry* **220** (2002) 69–85. doi:10.1016/s1387-3806(02)00823-0.

[18] Marciniak A, Despré V, Barillot T, Rouzée A, Galbraith M, Klei J, et al. XUV excitation followed by ultrafast non-adiabatic relaxation in PAH molecules as a femto-astrochemistry experiment. *Nature Communications* **6** (2015). doi:10.1038/ncomms8909.

[19] Bagdia C, Biswas S, Mandal A, Bhattacharjee S, Tribedi LC. Ionization and fragmentation of fluorene upon 250 keV proton impact. *The European Physical Journal D* **75** (2021). doi:10.1140/epjd/s10053-020-00001-7.

[20] Zhen J, Castillo SR, Joblin C, Mulas G, Sabbah H, Giuliani A, et al. Vuv photo-processing of pah cations: quantitative study on the ionization versus fragmentation processes. *The Astrophysical Journal* **822** (2016) 113. doi:10.3847/0004-637x/822/2/113.

[21] Bazzi S, Welsch R, Vendrell O, Santra R. Challenges in XUV photochemistry simulations: A case study on ultrafast fragmentation dynamics of the benzene radical cation. *The Journal of Physical Chemistry A* **122** (2018) 1004–1010. doi:10.1021/acs.jpca.7b11543.

[22] Reddy VS, Ghanta S, Mahapatra S. First principles quantum dynamical investigation provides evidence for the role of polycyclic aromatic hydrocarbon radical cations in interstellar physics. *Physical Review Letters* **104** (2010) 111102. doi:10.1103/physrevlett.104.111102.

[23] Domcke W, Yarkony DR. Role of conical intersections in molecular spectroscopy and photoinduced chemical dynamics. *Annual Review of Physical Chemistry* **63** (2012) 325–352. doi:10.1146/annurev-physchem-032210-103522.

[24] Galbraith MCE, Scheit S, Golubev NV, Reitsma G, Zhavoronkov N, Despré V, et al. Few-femtosecond passage of conical intersections in the benzene cation. *Nature Communications* **8** (2017). doi:10.1038/s41467-017-01133-y.

[25] Curchod BFE, Martínez TJ. Ab initio nonadiabatic quantum molecular dynamics. *Chemical Reviews* **118** (2018) 3305–3336. doi:10.1021/acs.chemrev.7b00423.

[26] Hervé M, Despré V, Nash PC, Loriot V, Boyer A, Scognamiglio A, et al. Ultrafast dynamics of correlation bands following XUV molecular photoionization. *Nature Physics* **17** (2020) 327–331. doi:10.1038/s41567-020-01073-3.

[27] Bernstein MP, Sandford SA, Allamandola LJ, Gillette JS, Clemett SJ, Zare RN. UV irradiation of polycyclic aromatic hydrocarbons in ices: Production of alcohols, quinones, and ethers. *Science* **283** (1999) 1135–1138. doi:10.1126/science.283.5405.1135.

[28] Boyer A, Hervé M, Despré V, Nash PC, Loriot V, Marciniak A, et al. Ultrafast vibrational relaxation dynamics in XUV-excited polycyclic aromatic hydrocarbon molecules. *Physical Review X* **11** (2021) 041012. doi:10.1103/physrevx.11.041012.

[29] Bouwman J, Cuppen HM, Steglich M, Allamandola LJ, Linnartz H. Photochemistry of polycyclic aromatic hydrocarbons in cosmic water ice. *Astronomy & Astrophysics* **529** (2011) A46. doi:10.1051/0004-6361/201015762.

[30] Ruehl E, Price SD, Leach S. Single and double photoionization processes in naphthalene between 8 and 35 eV. *The Journal of Physical Chemistry* **93** (1989) 6312–6321. doi:10.1021/j100354a011.

[31] Leach S, Eland JHD, Price SD. Formation and dissociation of dications of naphthalene-d8. *The Journal of Physical Chemistry* **93** (1989) 7583–7593. doi:10.1021/j100359a014.

[32] Lu J, Ren X, Cao L. Studies on characteristics and formation of soot nanoparticles in an ethylene/air inverse diffusion flame. *Journal of Energy Engineering* **142** (2016) 04015041. doi:10.1061/(asce)ey.1943-7897.0000305.

[33] Petrignani A, Vala M, Eyler JR, Tielens AGGM, Berden G, van der Meer AFG, et al. Breakdown products of gaseous polycyclic aromatic hydrocarbons investigated with infrared ion spectroscopy. *The Astrophysical Journal* **826** (2016) 33. doi:10.3847/0004-637x/826/1/33.

[34] Güsten H, Klasinc L, Marsel J, Milivojević D. A comparative study of the mass spectra of stilbene and fluorene. *Organic Mass Spectrometry* **6** (1972) 175–178. doi:10.1002/oms.1210060207.

[35] Bowie J, Bradshaw T. Electron impact studies. LVI. the fluorenyl and phenalenyl cations. the application of metastable characteristics. *Australian Journal of Chemistry* **23** (1970) 1431. doi:10.1071/ch9701431.

[36] Zhang W, Si Y, Zhen J, Chen T, Linnartz H, Tielens AGGM. Laboratory photochemistry of covalently bonded fluorene clusters: Observation of an interesting PAH bowl-forming mechanism. *The Astrophysical Journal* **872** (2019) 38. doi:10.3847/1538-4357/aafe10.

[37] Andrews H, Boersma C, Werner MW, Livingston J, Allamandola LJ, Tielens AGGM. Pah emission at the bright locations of pdrs: The grandpah hypothesis. *The Astrophysical Journal* **807** (2015) 99. doi:10.1088/0004-637x/807/1/99.

[38] Ackermann W, Asova G, Ayvazyan V, Azima A, Baboi N, Bähr J, et al. Operation of a free-electron laser from the extreme ultraviolet to the water window. *Nature Photonics* **1** (2007) 336–342. doi:10.1038/nphoton.2007.76.

[39] Erk B, Müller JP, Bomme C, Boll R, Brenner G, Chapman HN, et al. CAMP@FLASH: an end-station for imaging, electron- and ion-spectroscopy, and pump–probe experiments at the FLASH free-electron laser. *Journal of Synchrotron Radiation* **25** (2018) 1529–1540. doi:10.1107/s1600577518008585.

[40] Düsterer S, Rehders M, Al-Shemmary A, Behrens C, Brenner G, Brovko O, et al. Development of experimental techniques for the characterization of ultrashort photon pulses of extreme ultraviolet free-electron lasers. *Physical Review Special Topics - Accelerators and Beams* **17** (2014) 120702. doi:10.1103/physrevstab.17.120702.

[41] Behrens C, Gerasimova N, Gerth C, Schmidt B, Schneidmiller EA, Serkez S, et al. Constraints on photon pulse duration from longitudinal electron beam diagnostics at a soft x-ray free-electron laser. *Physical Review Special Topics - Accelerators and Beams* **15** (2012) 030707. doi:10.1103/physrevstab.15.030707.

[42] Redlin H, Al-Shemmary A, Azima A, Stojanovic N, Tavella F, Will I, et al. The FLASH pump–probe laser system: Setup, characterization and optical beamlines. *Nuclear Instruments and Methods in Physics Research Section A: Accelerators, Spectrometers, Detectors and Associated Equipment* **635** (2011) S88–S93. doi:10.1016/j.nima.2010.09.159.

[43] Eppink ATJB, Parker DH. Velocity map imaging of ions and electrons using electrostatic lenses: Application in photoelectron and photofragment ion imaging of molecular oxygen. *Review of Scientific Instruments* **68** (1997) 3477–3484. doi:10.1063/1.1148310.

[44] Parker DH, Eppink ATJB. Photoelectron and photofragment velocity map imaging of state-selected molecular oxygen dissociation/ionization dynamics. *The Journal of Chemical Physics* **107** (1997) 2357–2362. doi:10.1063/1.474624.

[45] Even U. "the even-lavie valve as a source for high intensity supersonic beam". *EPJ Techniques and Instrumentation* **2** (2015). doi:10.1140/epjti/s40485-015-0027-5.

[46] Clark AT, Crooks JP, Sedgwick I, Turchetta R, Lee JWL, John JJ, et al. Multimass velocity-map imaging with the pixel imaging mass spectrometry (PImMS) sensor: An ultra-fast event-triggered

camera for particle imaging. *The Journal of Physical Chemistry A* **116** (2012) 10897–10903. doi:10.1021/jp309860t.

[47] Amini K, Blake S, Brouard M, Burt MB, Halford E, Lauer A, et al. Three-dimensional imaging of carbonyl sulfide and ethyl iodide photodissociation using the pixel imaging mass spectrometry camera. *Review of Scientific Instruments* **86** (2015) 103113. doi:10.1063/1.4934544.

[48] Jaycen A. Open-source software compares abel transforms for easy use. *Scilight* **2019** (2019) 260003. doi:10.1063/1.5111853.

[49] Van Rossum G, Drake Jr FL. *Python reference manual* (Centrum voor Wiskunde en Informatica Amsterdam) (1995).

[50] Dahl DA, Delmore JE, Appelhans AD. SIMION PC/PS2 electrostatic lens design program. *Review of Scientific Instruments* **61** (1990) 607–609. doi:10.1063/1.1141932.

[51] [Dataset] Tikhonov DS. https://stash.desy.de/projects/cfa/repos/mcmcmcfitting/browse (2019).

[52] [Dataset] Steber A, Müller E. https://stash.desy.de/projects/cs/repos/pah/browse (2016).

[53] [Dataset] Tikhonov DS. https://stash.desy.de/projects/cfa/repos/campfancyanalysis/browse (2019).

[54] Pedersen S, Zewail AH. Femtosecond real time probing of reactions XXII kinetic description of probe absorption fluorescence depletion and mass spectrometry. *Molecular Physics* **89** (1996) 1455–1502. doi:10.1080/002689796173291.

[55] Tikhonov DS. *https://confluence.desy.de/display/CFA/CAMPFancyAnalyis+Home* (2019).

[56] Savelyev E, Boll R, Bomme C, Schirmel N, Redlin H, Erk B, et al. Jitter-correction for IR/UV-XUV pump-probe experiments at the FLASH free-electron laser. *New Journal of Physics* **19** (2017) 043009. doi:10.1088/1367-2630/aa652d.

[57] Schulz S, Grguraš I, Behrens C, Bromberger H, Costello JT, Czwalinna MK, et al. Femtosecond all-optical synchronization of an x-ray free-electron laser. *Nature Communications* **6** (2015). doi:10.1038/ncomms6938.

[58] Frasinski LJ, Codling K, Hatherly PA. Covariance mapping: A correlation method applied to multiphoton multiple ionization. *Science* **246** (1989) 1029–1031. doi:10.1126/science.246.4933.1029.

[59] Tikhonov DS. *https://confluence.desy.de/display/CFA/TOF-TOF+covariance+analysis* (2019).

[60] Dabestani R, Ivanov IN. A compilation of physical, spectroscopic and photophysical properties of polycyclic aromatic hydrocarbons. *Photochemistry and Photobiology* **70** (1999) 10–34. doi:10.1111/j.1751-1097.1999.tb01945.x.

[61] Holm AIS, Johansson HAB, Cederquist H, Zettergren H. Dissociation and multiple ionization energies for five polycyclic aromatic hydrocarbon molecules. *The Journal of Chemical Physics* **134** (2011) 044301. doi:10.1063/1.3541252.

[62] Vinitha M, Nair AM, Ramanathan K, Kadhane UR. Understanding dehydrogenation sequence in fluorene$^+$ by multiphoton ionisation-excitation processes. *International Journal of Mass Spectrometry* **471** (2022) 116704. doi:10.1016/j.ijms.2021.116704.

[63] Frasinski LJ. Covariance mapping techniques. *Journal of Physics B: Atomic, Molecular and Optical Physics* **49** (2016) 152004. doi:10.1088/0953-4075/49/15/152004.

[64] Slater CS, Blake S, Brouard M, Lauer A, Vallance C, John JJ, et al. Covariance imaging experiments using a pixel-imaging mass-spectrometry camera. *Physical Review A* **89** (2014) 011401. doi:10.1103/physreva.89.011401.

[65] Slater CS, Blake S, Brouard M, Lauer A, Vallance C, Bohun CS, et al. Coulomb-explosion imaging using a pixel-imaging mass-spectrometry camera. *Physical Review A* **91** (2015) 053424. doi:10.1103/physreva.91.053424.

[66] Vallance C, Heathcote D, Lee JWL. Covariance-map imaging: A powerful tool for chemical dynamics studies. *The Journal of Physical Chemistry A* **125** (2021) 1117–1133. doi:10.1021/acs.jpca.0c10038.

[67] West BJ, Lesniak L, Mayer PM. Why do large ionized polycyclic aromatic hydrocarbons not lose C_2H_2? *The Journal of Physical Chemistry A* **123** (2019) 3569–3574. doi:10.1021/acs.jpca.9b01879.